Nanoscale

PAPER

View Article Online
View Journal | View Issue

Check for updates

**Cite this:** *Nanoscale*, 2020, **12**, 5483

Published on 13 February 2020. Downloaded by Washington State University Libraries on 9/11/2020 6:13:46 AM.

# A wet-processed, binder-free sulfur cathode integrated with a dual-functional separator for flexible Li–S batteries†

Xuewei Fu,*[a] Francis Dunne,[a] Min Chen[a,b] and Wei-Hong Zhong *[a]

Received 30th December 2019,
Accepted 13th February 2020

DOI: 10.1039/c9nr10966h

rsc.li/nanoscale

Developing flexible, robust and lightweight sulfur cathodes by rationally designing their structures and configurations through a viable and scalable strategy is a critical enabler for fulfilling flexible lithium–sulfur (Li–S) batteries. However, besides the requirements for cathode flexibility, intrinsic limitations from the shuttling of lithium polysulfides and the growth of Li dendrites have restricted the widespread implementations of Li–S batteries. Here, we report a wet-processed strategy by dissolving and recrystallizing S in a suitable solvent to fabricate a flexible, binder-free S cathode. Integrating the resulting S cathode with a dual-functional separator has demonstrated to be able to suppress both the shuttle effect and growth of dendritic Li. The wet-processed strategy not only enables the fabrication of flexible and binder-free S-nanomat cathodes, but also facilitates the deposition of the cathodes on the separators. Meanwhile, a dual-functional separator is fabricated by vapor-phase polymerization of polypyrrole (PPy) coating on both surfaces of the commercial separator, which leads to the reduction of the shuttle effect and the suppression of the growth of dendritic Li simultaneously. As a result, by integrating the S-nanomat and the dual-functional separator, the cathode exhibits exceptional mechanical properties and electrochemical performance. Li–S pouch cells are further demonstrated to show stable cycling performance in the bending state, indicating the feasibility of the integrated S cathode for flexible Li–S batteries.

## 1. Introduction

Flexible and wearable electronics have emerged as advanced and next-generation energy storage devices that require decent mechanical flexibility. Among various types of energy storage systems, lithium–sulfur (Li–S) batteries have received increasing interest in recent years because of their exceptional attributes including high theoretical capacity of sulfur (1675 mA h g$^{-1}$), high energy density (2600 W h kg$^{-1}$) and low cost.[1–4] To achieve self-powered flexible Li–S batteries, fabrication of robust and flexible sulfur cathodes is a fundamental enabler. However, conventional electrode fabrication *via* casting slurries on metallic current collectors increases the overall battery weight and decreases the gravimetric energy density.[5–7] Therefore, to develop advanced future electronics, there is an urgent need for designing robust, flexible, and lightweight sulfur cathodes without compromising their electrochemical performance.

Despite the fact that Li–S batteries are promising rechargeable battery systems, their practical use is still limited by the inferior intrinsic properties and electrochemistry of the sulfur active material. It is known that the low electrical conductivity of sulfur, the shuttle effect of soluble lithium polysulfides ($Li_2S_n$, $3 \leq n \leq 8$), the large volume deformation, and the growth of Li dendrites are the typical issues that degrade the battery performance and even pose severe safety concerns.[8–11] Among these obstacles, resolving the shuttle effect and the growth of Li dendrites are believed to be the principal tasks to realize a safe and high-performance Li–S battery.[12–16] In an effort of creating flexible and lightweight Li–S batteries with improved performance, numerous studies have excluded the use of current collectors and created flexible free-standing sulfur cathodes by incorporating sulfur into conductive hosts such as carbon nanotubes,[17–19] graphene,[20,21] $Ti_3C_2T_x$ paper,[22] TiN/C naonfibers,[23] *etc*. The conductive hosts could not only buffer the strain from volume expansion, but also increase the electrical conductivity and help prevent the diffusion of lithium polysulfides.[24,25] However, more efforts are needed to further improve the mechanical properties of the free-standing sulfur cathodes in order to afford long-term deformations.

---

[a] *School of Mechanical and Materials Engineering, Washington State University, Pullman, WA 99164, USA. E-mail: xuewei.fu@wsu.edu, katie_zhong@wsu.edu*
[b] *College of Materials Science and Engineering, Chongqing University, 174 Shezhengjie, Chongqing, 400044, PR China*

† Electronic supplementary information (ESI) available. See DOI: 10.1039/C9NR10966H

Published on 13 February 2020. Downloaded by Washington State University Libraries on 9/11/2020 6:13:46 AM.

As an alternative to free-standing sulfur cathodes, integration of sulfur cathodes and separators represents an attractive configuration design. Benefiting from the intrinsically good mechanical flexibility of separators, recently emerging studies have directly deposited sulfur cathodes on separators as the substrates. The seamless cathode–separator configuration reduced the interfacial resistance and improved structural stability.[26,27] It has been revealed that the rational integration of the sulfur cathode and separator could lead to highly flexible Li–S batteries being able to withstand mechanical deformations. For example, Zhou *et al.*[27] cast sulfur–graphene slurries on a separator, resulting in excellent flexibility and high-energy-density Li–S batteries. Hsieh *et al.*[28] integrated sulfur cathodes with plasma-treated separators, which showed good mechanical integrity. In addition, with the aim of inhibiting the shuttle effect, many efforts have been made to modify the separator by incorporating an interlayer made of carbon nanofibers (CNFs),[29] $MnO_2$/CNTs,[26] *etc.*, between the cathode and separator to prevent the diffusion of lithium polysulfides. The aforementioned research provided significant insight into the design of integrated sulfur cathode–separator configurations leading to high-performance flexible Li–S batteries. The interlayers in these studies showed effectiveness at inhibiting the shuttle effect, but the inability of suppressing the growth of Li dendrites still remains a drawback.

To endow the flexible Li–S batteries with safety for making a leap to practical applications, developing effective strategies to stabilize Li metal anodes should be taken into consideration. Tremendous efforts have been devoted to suppressing the growth of Li dendrites by optimizing electrolytes,[30–32] creating an artificial solid electrolyte interphase (SEI),[33–35] building composite Li metal anodes,[36–38] modifying separators,[39–41] *etc.* Among these methods, modifying the separator would be a very appealing and durable solution, because the separator as a crucial interfacial component strongly impacts not only the diffusion of molecules (*e.g.* lithium polysulfides) but also the ion deposition kinetics. Therefore, adding the two functions (*i.e.* refraining the shuttle effect and suppressing the growth of Li dendrites) to the separators is expected to be able to enhance the electrochemical performance and safety of the batteries simultaneously.

In this study, we report a simple and scalable wet-processed strategy, *i.e.* a dissolution–recrystallization strategy, for fabricating flexible and binder-free sulfur cathodes integrated with dual-functional separators capable of suppressing the shuttle effect and stabilizing the Li metal anode. The wet-processed strategy not only enables the fabrication of a flexible binder-free sulfur-CNT nanomat as the cathode, but also facilitates the deposition of the cathode on the separator. The CNT bundles are prone to form 3D networked structures under appropriate treatment, which is a benefit to generate flexible sulfur cathodes. Meanwhile, the high electrical conductivity of CNTs helps increase the overall conductivity of the resulting sulfur cathodes. Moreover, a dual-functional separator modified with polypyrrole (PPy) coating on both surfaces of the commercial separator is fabricated *via* a vapor-phase polymerization method. This is because PPy as a conductive polymer is advantageous for inhibiting both the shuttle effect[42–44] and the growth of Li dendrites,[45] as well as facile synthesis. As a result, the sulfur nanomat-dual functional separator integrated cathode shows exceptional mechanical properties and electrochemical performance. In addition, a flexible Li–S battery is demonstrated to show stable cycling performance in the bending state, benefiting from the good mechanical flexibility of the integrated sulfur cathode.

## 2. Results and discussion

To achieve an integrated cathode–separator configuration, a facile and scalable strategy based on a dissolution–recrystallization process of sulfur followed by vacuum filtration was adopted in this study (Fig. 1(a)). Specifically, sulfur was first dissolved in *N*-methyl-2-pyrrolidone (NMP) solvent at 120 °C, which promptly formed an orange solution as shown in Fig. 1(a). The totally dissolved sulfur facilitates the formation of homogeneous sulfur electrode composites with conductive agents. CNTs were then dispersed in the sulfur solution, in which the sulfur molecules were thoroughly adsorbed by the CNT bundles. When cooling down the solution mixture, sulfur is recrystallized and deposited on CNTs. In the meantime, a commercial separator (CS), Celgard® 2400, was soaked in an $FeCl_3$ solution and then subjected to the vapor of pyrrole for initiating polymerization, which eventually resulted in the formation of conductive PPy coating on both sides of the separator (PPy@CS). The S/CNT dispersion mixture was vacuum filtered on the PPy@CS to generate the binder-free flexible S@CNT nanomat-PPy@CS integrated cathode. Fig. 1(b) illustrates the dual roles that the PPy@CS plays in the resulting batteries. As illustrated, conventional Li–S batteries suffer from the shuttling of polysulfides and the uncontrollable growth of dendritic Li due to the unstable deposition of $Li^+$ ions.[46,47] To synchronously overcome these two issues, a dual-functional separator, PPy@CS, was backed up with the S@CNT nanomat to result in the integrated sulfur cathode. The PPy that was grown on the surface of the separator helped to trap and convert the polysulfides while it regulated the $Li^+$ ion flux to stabilize the Li metal anode, which will be discussed in detail later.

Fig. 2(a) shows the XRD patterns of wet-processed sulfur in comparison with the pristine sulfur particles. The pristine orthorhombic sulfur and the wet-processed sulfur share the same diffraction peaks in the XRD patterns, which indicates that the dissolution–recrystallization process of sulfur does not change the crystalline structure of sulfur. Typical (113), (222) and (044) crystalline planes can be clearly found at the $2\theta$ positions of 15.7°, 23.3° and 31.7°,[48] respectively, for both samples. In addition, the CNTs exhibit a broad peak at around 26° indexed to the (002) peak.[49] For the S@CNTs, it can be seen that some typical peaks such as the (222) peak from sulfur are still present, but the peaks in the range of 30° to 70°

This journal is © The Royal Society of Chemistry 2020

Published on 13 February 2020. Downloaded by Washington State University Libraries on 9/11/2020 6:13:46 AM.

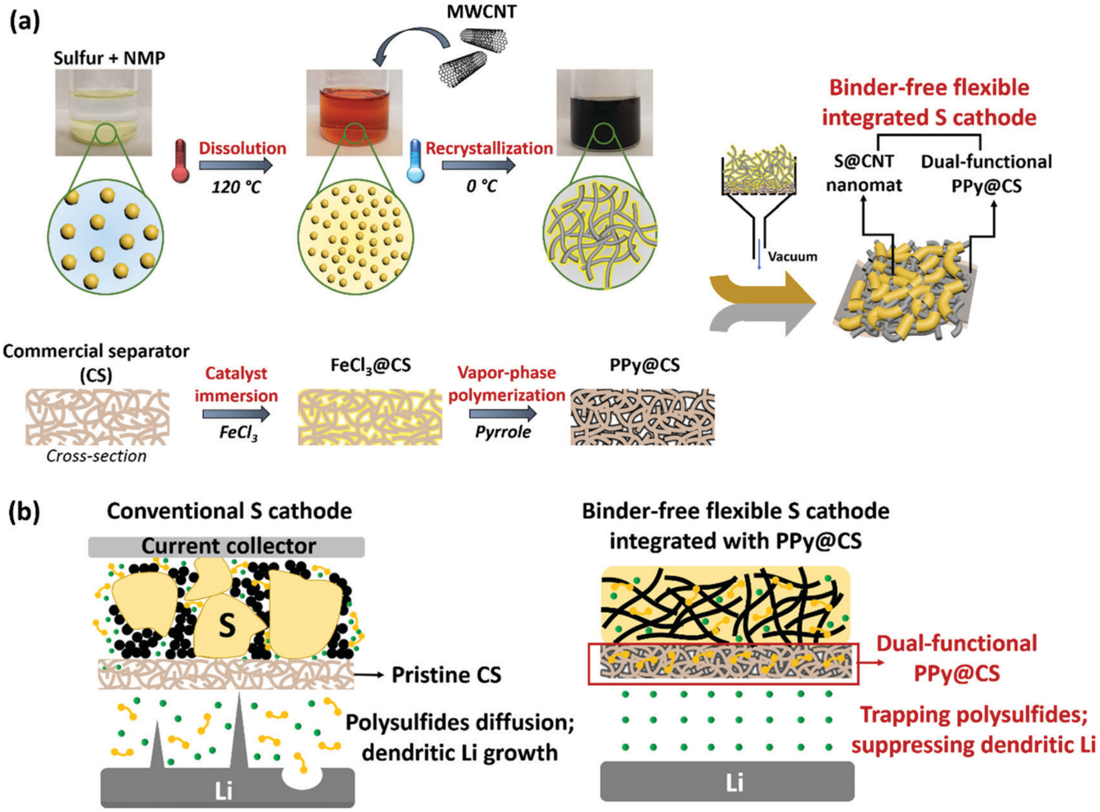

**Fig. 1** Schematic illustration of the fabrication of a S@CNT nanomat integrated with a dual-functional separator. (a) Fabrication of the integrated sulfur cathode. The sulfur cathode is fabricated *via* a dissolution–recrystallization strategy in which sulfur uniformly binds with the CNTs resulting in a sulfur-CNT nanomat (S@CNT). The dual-functional separator is fabricated by vapor-phase polymerization of PPy on both surfaces of the separator. The final integrated sulfur cathode is achieved by vacuum filtrating the S@CNT dispersion on the dual-functional separator. (b) Schematic showing the impacts of the dual-functional separator on trapping polysulfides and suppressing the growth of Li dendrites.

disappear, which may result from the shielding effect by CNTs. This result indicates that most sulfur is deposited into the CNT bundles. The SEM images in Fig. 2(b) indicate that the CNT bundles intertwine together forming a porous networked structure. If we take a closer look, the sulfur successfully coats on the CNT surface acting as a binder linking the CNT bundles, which warrants the film formation ability of the S@CNT nanomat. This is because in the fabrication process, CNTs are all dispersed in sulfur solution with an excessive amount of sulfur; therefore, some sulfur molecules are inevitably adsorbed on the CNT surface. It is worth noting that the entire S@CNT system is binder-free; thus, the unique sulfur-bound CNT networks help maintain the structural integrity of the resulting cathode. EDX mapping also confirms that sulfur is uniformly distributed throughout the CNT networks, which is facilitated in the dissolution–recrystallization process.

To reveal the loading of sulfur in the S@CNT nanomat, TGA analysis was carried out and the result is shown in Fig. 2(c). As is shown, compared with CNTs without a notable weight loss in the entire testing, the S@CNT nanomat undergoes a gradual weight loss starting from *ca.* 90 °C due to the loss of moisture, followed by a substantial weight loss ranging from *ca.* 150 °C to *ca.* 290 °C caused by the sublimation of sulfur.[50] Therefore, the loading of sulfur in the S@CNT nanomat is determined to be *ca.* 75 wt%. Meanwhile, a conventional sulfur cathode with the same weight ratio of sulfur/CNTs made by slurry-casting is fabricated for comparison (see details in the Experimental section), which is designated as the S-CNT mixture in the following text. As shown in Fig. 2(d), the S@CNT nanomat exhibits a much higher electrical conductivity of 16.7 S $m^{-1}$ than that of the S-CNT mixture (8.5 S $m^{-1}$). This results from the good structural uniformity of the S@CNT nanomat and the stable connection of the CNT conductive networks.

To simultaneously solve the two issues: shuttle effect and growth of Li dendrites, a dual-functional separator modified by PPy coating is designed and fabricated. As shown in Fig. 3(a), the pristine commercial separator (CS) shows a nanoporous structure with a pore size of about 100–200 nm. For the PPy@CS, it can be clearly seen that a coating layer is formed on the surface and the porous structure is still maintained, which warrants the smooth transfer of ions. To confirm the presence of PPy, FTIR spectra are recorded and shown in Fig. 3(b). For the pristine CS made of polypropylene (PP), characteristic peaks at 1459 and 1374 $cm^{-1}$ correspond to the C–H bending vibration of PP.[51] After modification by PPy,

Published on 13 February 2020. Downloaded by Washington State University Libraries on 9/11/2020 6:13:46 AM.

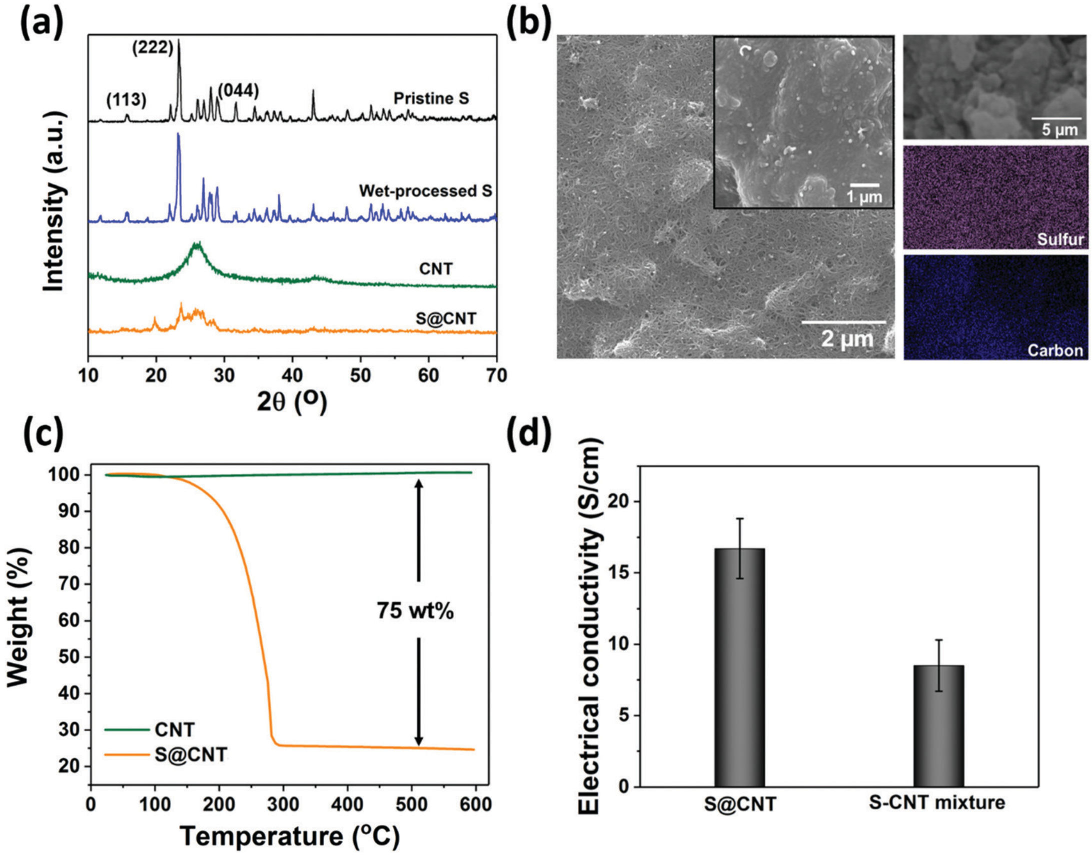

**Fig. 2** Morphological features and electrical properties of the S@CNT nanomat. (a) XRD patterns of wet-processed sulfur and the S@CNT. (b) SEM images and EDX mapping of the S@CNT nanomat. (c) TGA curves of the S@CNT compared with pure CNTs. (d) Electrical conductivity of the S@CNT compared with a conventional S-CNT mixture cathode.

several typical peaks at such as 1554, 1451 and 1044 cm$^{-1}$ contributed by the vibration of the Py ring, C–C stretching, and C–H in-plane vibration can be observed,[52,53] verifying the successful formation of PPy on the separator. It is interestingly found that the PPy coating improves the thermal stability of the separator. As shown in Fig. 3(c), pristine CS severely shrinks after exposure at 150 °C for 30 min, because the melting point of PP is about 160 °C.[54] In contrast, the PPy@CS exhibits much more slight shrinkage subjected to the same thermal treatment. This suggests that the PPy coating helps resist the thermal shrinkage because the melting point of PPy (>300 °C (ref. 55)) is much higher than that of PP. The increased thermal stability of the PPy@CS will allow the operation of the batteries at elevated temperatures and also improve the battery safety under the condition of thermal runaway.

In addition, it is revealed that the PPy@CS significantly reduces the shuttling of lithium polysulfides. A visualized diffusion testing is performed for the two separators shown in Fig. 3(d). As is shown, the lithium polysulfides quickly diffuse from the bottle filled with lithium polysulfide-containing electrolytes to the clean electrolyte side within only 5 minutes. The color of the clean electrolytes increases over time, which indicates that the lithium polysulfides continuously diffuse through the pristine CS because of the inability of CS to suppress the shuttling of lithium polysulfides. By contrast, for the PPy@CS system the diffusion of lithium polysulfides can be inhibited in the first 3 hours by the PPy@CS, and the lithium polysulfides start to penetrate the PPy@CS after 6 hours. This comparison implies that the PPy@CS plays a critical role in reducing the diffusion of lithium polysulfides due to the fact that PPy shows strong chemisorption of lithium polysulfides. This is because the nitrogen-containing groups of PPy can form Li–N interactions with lithium polysulfides.[42] Moreover, the ionic conductivity of the PPy@CS compared with the pure CS is shown in Fig. 3(e). The ionic conductivity of the PPy@CS is determined to be 2.1 × 10$^{-4}$ S cm$^{-1}$ that is higher than that of the CS (1.2 × 10$^{-4}$ S cm$^{-1}$). The improved ionic conductivity of the PPy@CS can be attributed to PPy's good affinity with Li$^+$ ions, because Li$^+$ ions can bind with the pyrrole ring by forming cation–π interactions.[45] The large conjugated system of PPy also allows the formation of continuous binding sites with Li$^+$ ions along the polymer chains, and therefore facilitates the transport of Li$^+$ ions. Benefiting from the good affinity with Li$^+$ ions, the interfacial stability against the Li metal is also improved by the PPy@CS. Fig. 3(f) shows the

Published on 13 February 2020. Downloaded by Washington State University Libraries on 9/11/2020 6:13:46 AM.

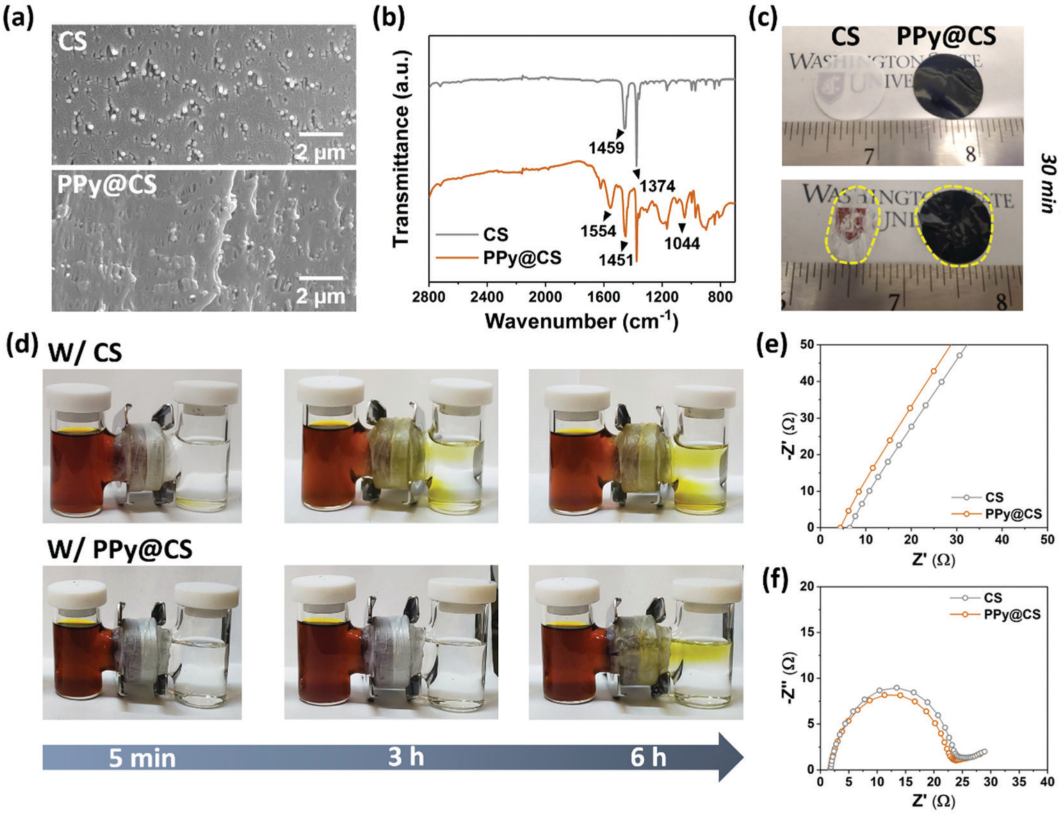

**Fig. 3** Physical and electrochemical properties of the PPy@CS. (a) Cross-sectional SEM images of a pristine CS and PPy@CS. (b) FTIR spectra of a pristine CS and PPy@CS. (c) Digital photos showing the thermal shrinkage of the two separators. (d) Diffusion testing of lithium polysulfides with a pristine CS and a PPy@CS. (e) Nyquist plots showing the ionic conductivity of the two separators conducted in stainless steel/separator/stainless steel configurations. (f) Nyquist plots showing the interfacial stability of the two separators against the Li metal conducted in Li/separator/Li configurations.

Nyquist plots of Li/separator/Li cells, consisting of a semicircle in the high-to-medium frequency region and a straight line in the low frequency region. The diameter of the semicircles on the real axis indicates the interfacial charge-transfer resistance of the separators. As is shown, the PPy@CS shows a lower interfacial charge-transfer resistance of *ca.* 22.3 Ω compared with 24.8 Ω for CS. The above results indicate that the PPy@CS is capable of suppressing the diffusion of lithium polysulfides and promoting the ion-transport process.

The electrochemical performance of the flexible and binder-free integrated sulfur cathode, S@CNT/PPy@CS, is evaluated in Li–S batteries. For comparison, the conventional sulfur cathode (S-CNT mixture) is also assembled into batteries. The representative cyclic voltammetry (CV) curves of the three sets of cells with different cathodes are shown in Fig. 4(a). In the cathodic scan, two reduction peaks can be observed due to the reduction of $S_8$ to long-chain lithium polysulfides ($Li_2S_n$, $4 \le n \le 8$), and further reduction to short-chain ones ($Li_2S_n$ or $Li_2S$), respectively.[56,57] In the anodic scan, two relatively close oxidation peaks are present, which emerge from the reverse transformation from insoluble short-chain lithium polysulfides to soluble long-chain ones and then to $S_8$, respectively.[58,59] It can be seen that all the three cells display well-defined reduction/oxidation peaks, indicating reversible electrochemical reactions. Specifically, the S@CNT/PPy@CS cell shows a pair of reduction peaks at 2.33 V and 2.03 V, and a pair of oxidation peaks at 2.33 V and 2.40 V, while the corresponding reduction and oxidation peaks of the S@CNT/CS cell are at 2.31, 2.01, 2.38, and 2.42 V, respectively. The difference between the corresponding reduction and oxidation potentials of the S@CNT/PPy@CS cell is much smaller than that of the S@CNT/CS cell, suggesting a better reaction reversibility and smaller polarization. This result indicates that the PPy@CS is able to promote the electrochemical reactions due to its higher ionic conductivity and effectiveness at suppressing the shuttle effect. However, it should also be noted that compared with the conventional sulfur cathode made of a S-CNT mixture, two S@CNT cathodes yield higher reduction potentials and lower oxidation potentials and therefore better reaction reversibility, which indicates that the wet-processed binder-free integrated sulfur cathodes are advantageous for delivering smooth electrochemical reactions. Fig. 4(b) displays the CV curves of the S@CNT/PPy@CS cell at varying scan rates. It can be seen that the peak currents increase with the scan rate with slight deviation of peak potentials, and the peaks are still evidently present even at a high scan rate of 0.5 mV s$^{-1}$. This indicates

Published on 13 February 2020. Downloaded by Washington State University Libraries on 9/11/2020 6:13:46 AM.

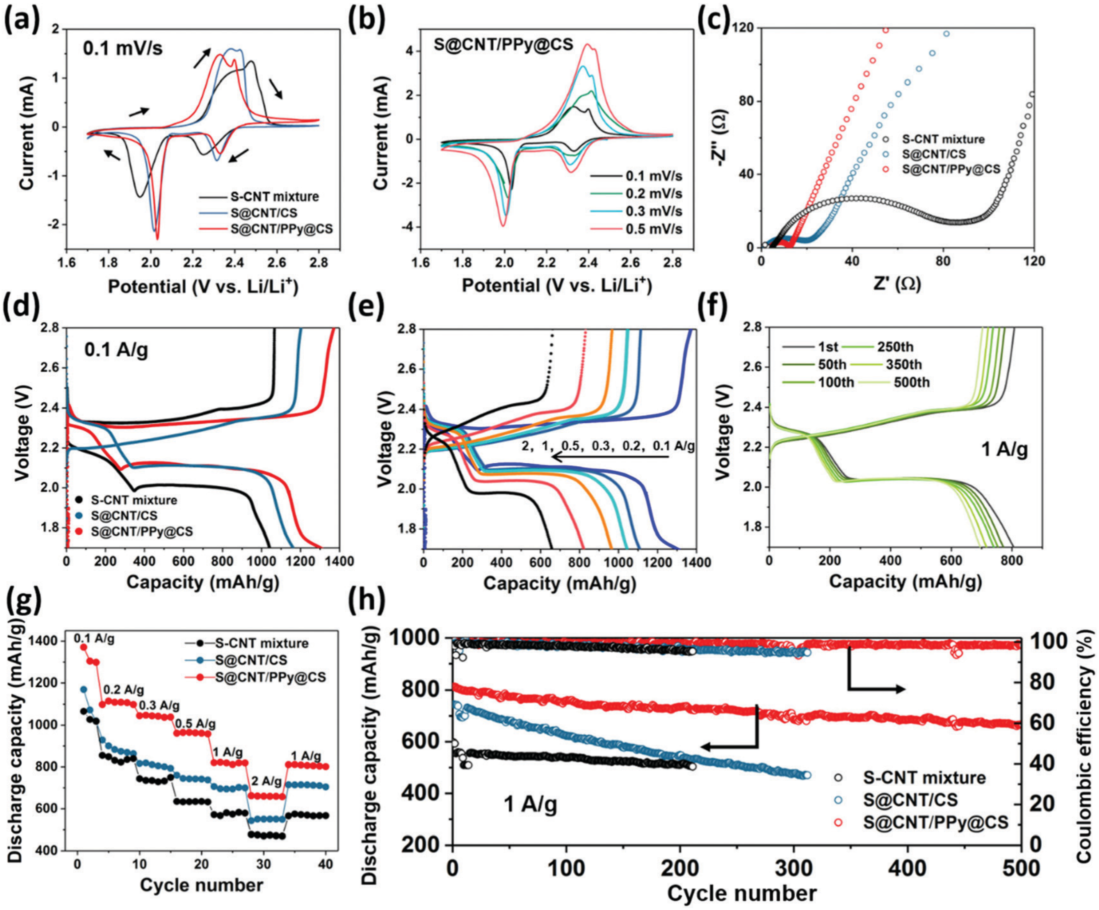

**Fig. 4** Electrochemical performance of Li–S batteries. (a) CV curves of different Li–S battery systems. (b) CV curves of Li–S batteries with the integrated sulfur cathode: S@CNT/PPy@CS. (c) Nyquist plots of different Li–S battery systems. (d) Voltage profiles of different Li–S battery systems at 0.1 A $g^{-1}$. (e) Voltage profiles of S@CNT/PPy@CS at varying current densities. (f) Voltage profiles of S@CNT/PPy@CS in different cycling numbers at 1 A $g^{-1}$. (g) Rate performance and (h) cycling stability of different Li–S battery systems.

that the cell affords stable and reversible electrochemical reactions at varying scan rates.

Fig. 4(c) shows the Nyquist plots of the various Li–S cells. It clearly shows that the two S@CNT cells have significantly smaller charge-transfer resistance compared with the S-CNT mixture cathode, as indicated by the diameter of the semicircle across the real axis. In specific, the S@CNT/PPy@CS shows the lowest charge-transfer resistance of *ca.* 8.4 Ω among the S@CNT/CS (19.7 Ω) and S-CNT mixture (84.3 Ω) cells. This result implies that the higher electrical conductivity of the two S@CNT cathodes as discussed above effectively reduces the interfacial resistance. Meanwhile, the PPy@CS is another enabler for further improving the kinetics of ion-transport owing to its high ionic conductivity and good interfacial stability with the Li metal. The low charge-transfer resistance of the S@CNT/PPy@CS cell is a benefit for yielding high electrochemical performance especially rate performance.

The voltage profiles of the various cells are presented in Fig. 4(d). At 0.1 A $g^{-1}$, the S@CNT/PPy@CS cell delivers the highest discharge capacity of 1308 mA h $g^{-1}$ compared with the S@CNT/CS cell (1170 mA h $g^{-1}$) and the S-CNT mixture cell (1038 mA h $g^{-1}$). This indicates that as compared with the S-CNT mixture cathode, the good structural uniformity and high electrical conductivity of the two S@CNT cathodes lead to higher utilization of sulfur active materials. More importantly, the PPy@CS is effective at alleviating the diffusion of lithium polysulfides such that the capacity is increased, which is in good agreement with the above result in Fig. 3(d). The voltage profiles of the S@CNT/PPy@CS cell at various current densities are shown in Fig. 4(e). It is found that from 0.1 to 1 A $g^{-1}$, the second discharge plateaus only slightly drop down and are still smooth. Interestingly, at increased current rates such as 0.2 A $g^{-1}$, the polarization even decreases compared with the case of 0.1 A $g^{-1}$. It is speculated that the PPy@CS may need a longer time to be fully wetted, and thus the S@CNT/PPy@CS cell needs a longer activation time. Upon further increasing the current density to 2 A $g^{-1}$, the flat discharge plateau decreases to *ca.* 1.9 V. This result indicates that the S@CNT/PPy@CS cell affords stable and reversible electrochemical reactions even at high current densities, benefiting from its good structural properties, fast charge-transfer and suppressed shuttling of lithium polysulfides. To further prove

This journal is © The Royal Society of Chemistry 2020

Published on 13 February 2020. Downloaded by Washington State University Libraries on 9/11/2020 6:13:46 AM.

this point, the various cycling numbers of voltage profiles at a high current density of 1 A $g^{-1}$ are present in Fig. 4(f). As is shown, from the first to the 500th cycles, the voltage profiles having good overlap are very smooth and show slight capacity decay, which suggests a stable long-term charging–discharging process.

The rate performance of the Li–S cells is compared to further reveal the advantages of the S@CNT/PPy@CS cell. It is clearly seen that the S@CNT/PPy@CS cell shows the highest capacities at all tested current densities among the three cells. To be more specific, the capacities of the S@CNT/PPy@CS cell are 1110, 1039, 961, 808 and 662 mA h $g^{-1}$ at 0.2, 0.3, 0.5, 1 and 2 A $g^{-1}$, respectively, compared with 883, 805, 742, 695 and 544 mA h $g^{-1}$ for the S@CNT/CS cell. The S-CNT mixture cathode is even inferior to the S@CNT/CS cell. When switching the current density back to 1 A $g^{-1}$, a reversible capacity of 807 mA h $g^{-1}$ is achieved for the S@CNT/PPy@CS cell, which suggests that the cell can deliver high capacities without notable capacity loss over varying current densities. Moreover, the S@CNT/PPy@CS cell shows exceptional cycling performance in Fig. 4(h). In comparison with the cells with the S-CNT mixture and S@CNT/CS, the S@CNT/PPy@CS yields the highest and stable capacities in 500 cycles at 1 A $g^{-1}$. In contrast, the cell with the S@CNT/CS shows evidently continuous capacity decay during the cycling process, which is caused by the gradual diffusion of lithium polysulfides out of the cathode. Although the CNT frameworks have some effect in suppressing the diffusion of lithium polysulfides, the long-term performance remains an issue without a "secondary-guard". Thus, the S-CNT mixture cell experiences a dramatic capacity loss in the first 20 cycles and then the capacities stabilize at around 540 mA h $g^{-1}$. This is because the lithium polysulfides quickly dissolve and diffuse in the electrolytes causing a great loss of sulfur, and then the equilibrium state is reached. The capacity decay rate of the S@CNT/PPy@CS cell is as low as 0.037% as compared with 0.12% and 0.084% for S@CNT/CS and S-CNT mixture cells, respectively. The average coulombic efficiencies of the S@CNT/PPy@CS, S@CNT/CS and S-CNT mixture cells are 99.2%, 98.1% and 98.3%, respectively. The superior cycling stability and coulombic efficiency of the S@CNT/PPy@CS cell are contributed by the synergistic effect from the CNT-intertwined networked structure of the S@CNT cathode and the polysulfide-adsorption function of the PPy@CS.

To demonstrate the effectiveness of the PPy@CS at suppressing the growth of Li dendrites, the Li plating/stripping behaviors of the two separators are studied in Li/Cu cells. As shown in Fig. 5(a), at a current rate of 0.5 mA $cm^{-2}$ and a deposition capacity of 1 mA h $cm^{-2}$, the cell with the pristine CS shows fluctuated voltage profiles, indicating unstable deposition of the Li on Cu electrode.[60,61] In contrast, the PPy@CS cell yields much more stable voltage profiles and lower polarization for *ca.* 320 hours, which suggests that the deposition of Li on a Cu electrode is stable leading to the formation of a thin and uniform SEI. Meanwhile, the coulombic efficiency of the PPy@CS cell (about 97%) is much higher and more stable than that of the CS cell shown in Fig. 5(b), implying that the deposited Li on the Cu electrode can be almost completely stripped without breaking the SEI layer. Furthermore, regarding the specific voltage profiles of the cells at certain cycles, one finds that both PPy@CS and CS cells show smooth plating/stripping plateaus (Fig. 5(c) and (d)). However, it

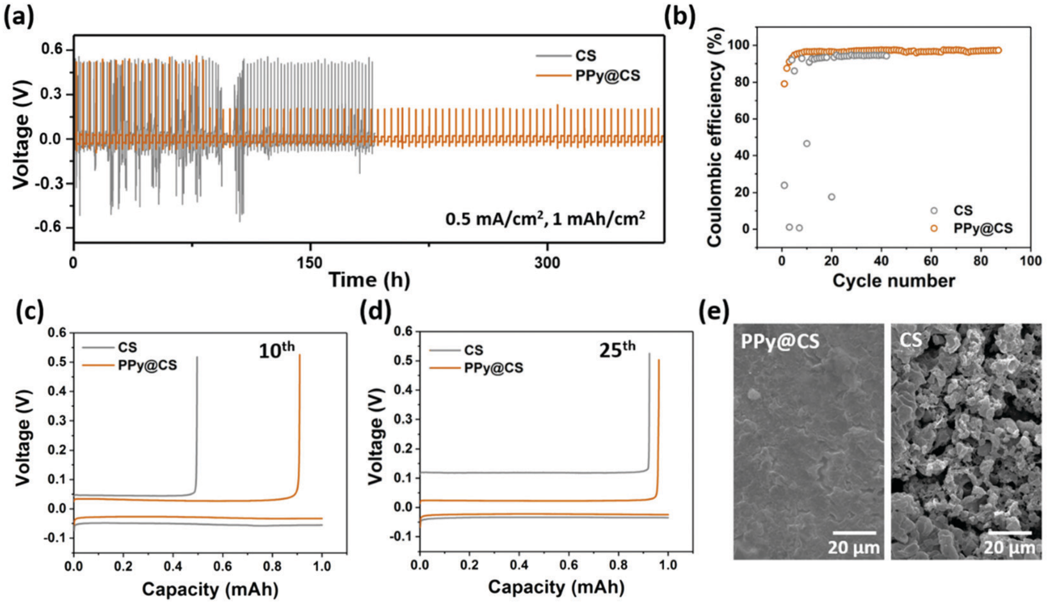

**Fig. 5** Li plating/stripping behavior studies of the PPy@CS. (a) Voltage profiles of Li plating/stripping behavior in Li/Cu cells with different separators. (b) Coulombic efficiency of Li/Cu cells with different separators. (c) and (d) Voltage profiles of Li/Cu cells at the 10th and the 25th cycles. (e) SEM images of the Cu electrode after 30 cycles.

Published on 13 February 2020. Downloaded by Washington State University Libraries on 9/11/2020 6:13:46 AM.

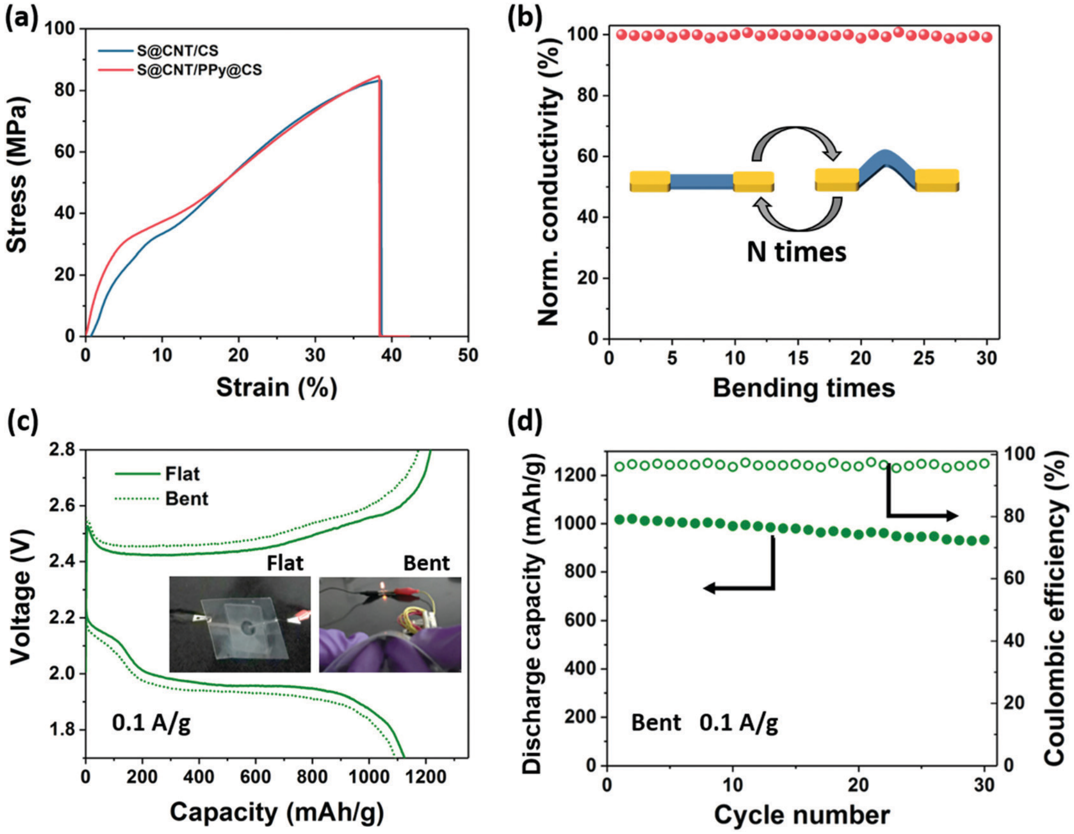

**Fig. 6** Electrochemical performance of flexible Li–S batteries. (a) Strain–stress curves of S@CNT/CS and S@CNT/PPy@CS cathodes. (b) Normalized electrical conductivity of the S@CNT/PPy@CS *versus* bending times. (c) Voltage profiles of the flexible Li–S battery in flat and bent states. (d) Cycling performance of the flexible Li–S battery in the bending state.

clearly shows that the potential hysteresis of the PPy@CS cell is much lower than that of the CS cell. For example, at the 25th cycle (Fig. 5(d)), the potential hysteresis of the PPy@CS cell is only *ca.* 44 mV, compared with *ca.* 154 mV for the CS cell. The much lower potential hysteresis of the PPy@CS cell results from the homogeneous ion-deposition and the formation of a thin and stable SEI layer.[62,63]

After cycling testing, the cells were disassembled, and the morphologies of the cycled Cu electrode were examined. As shown in Fig. 5(e), the Cu electrode with CS shows numerous dendritic Li and dead Li species, and many cracks are generated on the surface. In contrast, the Cu surface is much smoother without cracks or Li dendrites for the case of PPy@CS, which indicates that the SEI layer is stable and the continuous plating/stripping of Li does not destroy the SEI layer. The stable Li plating/stripping performance of the PPy@CS cell can be contributed by the role of PPy in regulating and stabilizing the $Li^+$ ion flux. As discussed above, the PPy coating on the separator is able to bind with $Li^+$ ions to not only facilitate the transport of $Li^+$ ions, but also regulate the ion flux passing through the separator. As a result, the PPy@CS plays a critical role in stabilizing the deposition of $Li^+$ ions and therefore suppressing the growth of Li dendrites.

Good mechanical properties of the integrated sulfur cathode are a guarantee for sustaining the continuous mechanical deformations of flexible Li–S batteries. The strain–stress curves of the integrated sulfur cathodes testing the machine direction are shown in Fig. 6(a). Both the S@CNT/PPy@CS and S@CNT/CS samples undergo a linear elastic deformation in the first step. The two electrode samples can withstand a stress higher than 20 MPa. The elastic strain of the S@CNT/PPy@CS is 6.2% while the value of the S@CNT/CS is slightly higher *i.e.* 8.6%. The fracture stress and strain of the two samples are quite comparative, which are about 84.7 MPa and 38.3% for the S@CNT/PPy@CS, and 83.1 MPa and 38.5% for the S@CNT/CS. The high mechanical properties of the integrated electrodes are mainly contributed by the beneficial separator providing robust mechanical support. In addition, the tolerance of the integrated electrodes under deformations is tested *via* measuring the electrical conductivity under continuous bending/unbending states. As shown in Fig. 6(b), the dynamic bent/flat cycling has no significant impact on the S@CNT/PPy@CS electrode, as indicated by the stable normalized electrical conductivity for 30 cycles of the bending/unbending process with a bending angle of 90°. The high stability of the electrical conductivity is a result of good structural stability of the S@CNT nanomat and the integration of the electrode configuration, which helps maintain stable

This journal is © The Royal Society of Chemistry 2020

Published on 13 February 2020. Downloaded by Washington State University Libraries on 9/11/2020 6:13:46 AM.

electrochemical performance of the resulting Li–S battery in the deformation state.

Furthermore, we assembled pouch cells using the integrated S@CNT/PPy@CS cathode and Li foil as the anode, to demonstrate the feasibility of the integrated cathode for flexible batteries. As shown in the insets of Fig. 6(c), in the bending state, the pouch cell is still able to power the LED light indicating a normal operation of the cell. Regarding the charge–discharge curves in Fig. 6(c), one finds that in the flat state, the discharge capacity is 1124 mA h $g^{-1}$ at 0.1 A $g^{-1}$ and the second discharge plateau is 1.95 V, much lower than the theoretical one at *ca.* 2.15 V.[64] In the bending state, the discharge capacity is slightly decreased to 1094 mA h $g^{-1}$, because of the poor contact of the battery components possibly. Meanwhile, a cyclic testing was performed on the bent pouch cell with a bending angle of 90°. As shown in Fig. 6(d), the pouch cell delivers an initial discharge capacity of 1016 mA h $g^{-1}$ and then decays to 932 mA h $g^{-1}$ after 30 cycles at 0.1 A $g^{-1}$, with an average coulombic efficiency of 97.5%. Although the performance is not as good as the coin-type cells as studied in Fig. 4, we believe that by reforming the battery packaging and sealing technologies, it is expected that a high-performance and durable pouch cell can be achieved.

# 3. Conclusion

In summary, we report a dissolution–recrystallization strategy for fabricating a robust, flexible and binder-free S cathode integrated with a dual-functional separator enabling to suppress both the shuttle effect and the growth of Li dendrites. The dissolution–recrystallization strategy not only leads to uniform adsorption of S on CNT networks and then formation of a robust S@CNT nanomat, but also helps the deposition of the nanomat on the separator. The dual-functional separator, which is made by vapor-phase polymerization of PPy on both sides of the commercial separator, enables the suppression of the shuttle effect and prevent the growth of Li dendrites simultaneously. This is because PPy shows chemisorption of lithium polysulfides and strong binding with $Li^+$ ions for homogenizing the ion-deposition. By integrating the S@CNT nanomat and the dual-functional separator, the resulting S cathode shows good mechanical properties and excellent electrochemical performance, *e.g.* 0.037% decay rate for 500 cycles at 1 A $g^{-1}$. Furthermore, we demonstrate that the pouch cells with the integrated S cathode yield stable cycling performance in the bending state, which verifies the feasibility of the S cathode for realization of flexible Li–S batteries. This study proposes a viable and scalable strategy for fabricating robust and integral electrode structures leading to flexible and wearable electronic devices.

# 4. Experimental methods

## 4.1. Sample preparation

**Preparation of S@CNT nanomats.** The S@CNT nanomat was prepared by dissolving S powders (Sigma Aldrich) in NMP solvent (VWR) at 120 °C under vigorous stirring for 20 minutes. The content of S was kept constant to be 6 wt%. In the meantime, CNTs (multiwalled, Nanocyl SA) were dispersed in NMP solvent with a solid content of 0.5 wt%, which were treated by using a tip sonifier (Branson 250, magnitude: 15%) for 1 hour in an ice bath. Afterwards, the CNT dispersion was added to the above S solution and the mixture underwent another 20 minute-stirring at 120 °C. The weight ratio of S : CNTs is 75 : 25. The mixture was then cooled down at 0 °C in an ice bath for subsequent experiments.

**Preparation of dual-functional separators.** The dual-functional separators were fabricated by vapor-phase polymerization of PPy on commercial separators (Celgard® 2400). Briefly, the commercial separators were soaked in a solution of 0.1 M $FeCl_3$/ethanol for 1 hour. Excessive $FeCl_3$ solution was wiped with Kimwipes® tissue. The separators were then subjected to the pyrrole (Sigma Aldrich) monomer vapor in an air-tight bottle for 4 hours, in which the treated separators were placed above the pyrrole monomer allowing the vapor penetration through the separators. The final PPy treated separators (PPy@CS) were vacuum dried at 60 °C for 12 hours.

**Preparation of S@CNT/PPy@CS integrated cathodes.** The integrated S cathodes were prepared by vacuum filtration of the above S/CNT mixture dispersions on the PPy@CS separators. For the control sample, the mixture dispersions were filtered on pristine commercial separators. The loading of S active materials is around 1.8–2 mg.

**Preparation of conventional S cathodes.** The conventional S cathodes were prepared by a slurry-casting method. The compositions include 67.5 wt% S, 22.5 wt% CNTs and 10 wt% polyvinylidene fluoride (PVDF) as the binder. The mixture was bowl-milled for 30 minutes in NMP solvent until homogeneous electrode slurries were formed. The slurries were cast on carbon-coated aluminum foil using a doctor blade to control the thickness. The cast slurries were dried at room temperature for 6 hours and then transferred to a vacuum oven at 50 °C for 12 hours for removing residual moisture and solvents. The loading of S active materials was kept to be 1.8 mg.

**Assembly of Li–S cells.** The prepared integrated or conventional electrodes were punched into 0.5 inch circular disks for assembling cells. Coin-type (CR 2032) cells were assembled in an Ar-filled glovebox with the prepared S cathodes by using a liquid electrolyte solution composed of 1 M LiTFSI dissolved in a solvent mixture of DOL/DME (1 : 1 by volume) with 2 wt% $LiNO_3$ as the additive. The electrolyte/S ratio was kept to be 12 μL $mg^{-1}$. For assembling the pouch cells, the integrated S cathode and Li foil along with the electrolyte were sealed in plastic sheets using a Scotch® laminator.

## 4.2. Material characterization

**Morphological and mechanical property characterization.** The morphologies of the samples were investigated by scanning electron microscopy (SEM, Quanta 200F). Energy-dispersive X-ray spectroscopy (EDX) was conducted by using a Tescan Vega3 SEM. The crystalline structures were investigated by

Published on 13 February 2020. Downloaded by Washington State University Libraries on 9/11/2020 6:13:46 AM.

X-ray Diffraction (XRD) (Rigaku Miniflex 600) using Cu Kα radiation over a range of 10–70°. Fourier-transform infrared spectroscopy (FTIR) spectra were recorded by using a Nicolet iS10 with an ATR mode. The mechanical properties of the electrodes were determined using a universal testing machine (Instron, 5565A) with a tensile rate of 1 cm $\min^{-1}$. The thermal properties of the electrodes were studied by thermogravimetric analysis (TGA, TA Instruments) under a $N_2$ atmosphere at a heating rate of 10 °C $\min^{-1}$.

**Electrochemical measurements.** The electrical conductivity of the electrodes was measured using a four-probe method with a SourceMeter (Keithley 2410). The charge/discharge voltage profiles, cyclic stability and rate capability of the Li–S cells were obtained *via* cycling the cells with a cut-off voltage of 1.7–2.8 V using a battery analyzer (BST8-MA, MTI) at room temperature. The electrochemical impedance spectroscopy (EIS) spectra and the cyclic voltammetry (CV) curves of the Li–S cells were analyzed by using an electrochemical workstation (Bio-Logic) in a frequency range of 0.01–1 M Hz, and in the window of 1.7–2.8 V at various scan rates, respectively.

## Conflicts of interest

There are no conflicts to declare.

## Acknowledgements

The authors would like to gratefully acknowledge the financial support from the NSF CBET 1929236. The support on microscopy characterization from the Franceschi Microscopy & Imaging Center at Washington State University is also acknowledged.

## References

1 Y. Ye, F. Wu, S. Xu, W. Qu, L. Li and R. Chen, *J. Phys. Chem. Lett.*, 2018, **9**, 1398.

2 X. Li and X. Sun, *Adv. Funct. Mater.*, 2018, **28**, 1.

3 Z. W. Seh, Y. Sun, Q. Zhang and Y. Cui, *Chem. Soc. Rev.*, 2016, **45**, 5605.

4 X. Fu, C. Li, Y. Wang, L. Scudiero, J. Liu and W. H. Zhong, *J. Phys. Chem. Lett.*, 2018, **9**, 2450.

5 R. Shah, J. Y. Gu, A. A. Razzaq, X. Zhao, X. W. Shen, L. Miao, C. L. Yan, Y. Peng and Z. Deng, *ACS Appl. Energy Mater.*, 2018, **1**, 3171.

6 L. Hu, H. Wu, F. La Mantia, Y. Yang, Y. Cui and F. La Mantia, *ACS Nano*, 2010, **4**, 5843.

7 Y. kyu Park, G. gyung Park, J. gi Park and J. won Lee, *Electrochim. Acta*, 2017, **247**, 371.

8 M. Wild, L. O'Neill, T. Zhang, R. Purkayastha, G. Minton, M. Marinescu and G. J. Offer, *Energy Environ. Sci.*, 2015, **8**, 3477.

9 S. Zhang, K. Ueno, K. Dokko and M. Watanabe, *Adv. Energy Mater.*, 2015, **5**, 1500117.

10 X. Fu, Y. Wang, J. Tuba, L. Scudiero and W.-H. Zhong, *Small Methods*, 2018, **2**, 1800066.

11 M. R. Kaiser, Z. Han, J. Liang, S. X. Dou and J. Wang, *Energy Storage Mater.*, 2019, **19**, 1.

12 L. Fan, S. Chen, J. Zhu, R. Ma, S. Li, R. Podila, A. M. Rao, G. Yang, C. Wang, Q. Liu, Z. Xu, L. Yuan, Y. Huang and B. Lu, *Adv. Sci.*, 2018, **5**, 1.

13 X. Fu, Y. Wang, L. Scudiero and W. H. Zhong, *Energy Storage Mater.*, 2018, **15**, 447–457.

14 C. Yan, X. Q. Zhang, J. Q. Huang, Q. Liu and Q. Zhang, *Trends Chem.*, 2019, **1**, 693.

15 N. Xu, T. Qian, X. Liu, J. Liu, Y. Chen and C. Yan, *Nano Lett.*, 2017, **17**, 538.

16 T. Yang, T. Qian, J. Liu, N. Xu, Y. Li, N. Grundish, C. Yan and J. B. Goodenough, *ACS Nano*, 2019, **13**, 9067.

17 A. Mentbayeva, A. Belgibayeva, N. Umirov, Y. Zhang, I. Taniguchi, I. Kurmanbayeva and Z. Bakenov, *Electrochim. Acta*, 2016, **217**, 242.

18 Y. Z. Zhang, Z. Zhang, S. Liu, G. R. Li and X. P. Gao, *ACS Appl. Mater. Interfaces*, 2018, **10**, 8749.

19 M. R. Kaiser, X. Liang, H. K. Liu, S. X. Dou and J. Z. Wang, *Carbon*, 2016, **103**, 163.

20 M. Xiang, L. Yang, Y. Zheng, J. Huang, P. Jing, H. Wu, Y. Zhang and H. Liu, *J. Mater. Chem. A*, 2017, **5**, 18020.

21 K. Han, Z. Liu, J. Shen, Y. Lin, F. Dai and H. Ye, *Adv. Funct. Mater.*, 2015, **25**, 455.

22 H. Tang, W. Li, L. Pan, K. Tu, F. Du, T. Qiu, J. Yang, C. P. Cullen, N. McEvoy and C. (John) Zhang, *Adv. Funct. Mater.*, 2019, **29**, 1.

23 Y. Liao, J. Xiang, L. Yuan, Z. Hao, J. Gu, X. Chen, K. Yuan, P. K. Kalambate and Y. Huang, *ACS Appl. Mater. Interfaces*, 2018, **10**, 37955.

24 G. C. Li, G. R. Li, S. H. Ye and X. P. Gao, *Adv. Energy Mater.*, 2012, **2**, 1238.

25 M. Rao, X. Song and E. J. Cairns, *J. Power Sources*, 2012, **205**, 474.

26 M. Yao, R. Wang, Z. Zhao, Y. Liu, Z. Niu and J. Chen, *ACS Nano*, 2018, **12**, 12503.

27 G. Zhou, L. Li, D. W. Wang, X. Y. Shan, S. Pei, F. Li and H. M. Cheng, *Adv. Mater.*, 2015, **27**, 641.

28 Y. Y. Hsieh, L. Zhang, D. DeArmond, S. N. Kanakaraj, P. K. Adusei, N. T. Alvarez, Y. Fang, J. Daum and V. Shanov, *Carbon*, 2018, **139**, 1093.

29 S. Y. Lee, J. H. Kim, Y. H. Lee, S. J. Cho, J. G. Gwon, H. J. Cho, M. Jang and S. Y. Lee, *Energy Environ. Sci.*, 2019, **12**, 177.

30 C.-Z. Zhao, X.-Q. Zhang, X.-B. Cheng, R. Zhang, R. Xu, P.-Y. Chen, H.-J. Peng, J.-Q. Huang and Q. Zhang, *Proc. Natl. Acad. Sci. U. S. A.*, 2017, **114**, 11069.

31 J. Zheng, M. H. Engelhard, D. Mei, S. Jiao, B. J. Polzin, J. Zhang and W. Xu, *Nat. Energy*, 2017, **2**, 17012.

32 J. Yan, J. Yu and B. Ding, *Adv. Mater.*, 2018, **30**, 1705105.

33 Y. Liu, D. Lin, P. Y. Yuen, K. Liu, J. Xie, R. H. Dauskardt and Y. Cui, *Adv. Mater.*, 2017, **29**, 1605531.

34 K. Deng, D. Han, S. Ren, S. Wang, M. Xiao and Y. Meng, *J. Mater. Chem. A*, 2019, **7**, 13113.

This journal is © The Royal Society of Chemistry 2020

Published on 13 February 2020. Downloaded by Washington State University Libraries on 9/11/2020 6:13:46 AM.

35 Y. Nan, S. Li, B. Li and S. Yang, *Nanoscale*, 2019, **11**, 2194.

36 D. Lin, J. Zhao, J. Sun, H. Yao, Y. Liu, K. Yan and Y. Cui, *Proc. Natl. Acad. Sci. U. S. A.*, 2017, **114**, 4613.

37 Z. Liang, D. Lin, J. Zhao, Z. Lu, Y. Liu, C. Liu, Y. Lu, H. Wang, K. Yan, X. Tao and Y. Cui, *Proc. Natl. Acad. Sci. U. S. A.*, 2016, **113**, 2862.

38 J. Lang, Y. Jin, X. Luo, Z. Liu, J. Song, Y. Long, L. Qi, M. Fang, Z. Li and H. Wu, *J. Mater. Chem. A*, 2017, **5**, 19168.

39 C. Z. Zhao, P. Y. Chen, R. Zhang, X. Chen, B. Q. Li, X. Q. Zhang, X. B. Cheng and Q. Zhang, *Sci. Adv.*, 2018, **4**, 1.

40 S. S. Zhang, X. Fan and C. Wang, *J. Mater. Chem. A*, 2018, **6**, 10755.

41 Y. Liu, S. Xiong, J. Wang, X. Jiao, S. Li, C. Zhang, Z. Song and J. Song, *Energy Storage Mater.*, 2019, **19**, 24.

42 W. Li, Q. Zhang, G. Zheng, Z. W. Seh, H. Yao and Y. Cui, *Nano Lett.*, 2013, **13**, 5534.

43 F. Li, M. Rejaul, J. Ma, Z. Guo, H. Liu and J. Wang, *Energy Storage Mater.*, 2018, **13**, 312.

44 M. R. Kaiser, Z. Han and J. Wang, *J. Power Sources*, 2019, **437**, 226925.

45 Z. Wen, Y. Peng, J. Cong, H. Hua, Y. Lin, J. Xiong, J. Zeng and J. Zhao, *Nano Res.*, 2019, **12**, 2535.

46 D. Lin, Y. Liu and Y. Cui, *Nat. Nanotechnol.*, 2017, **12**, 194.

47 M. D. Tikekar, L. A. Archer and D. L. Koch, *J. Electrochem. Soc.*, 2014, **161**, A847–A855.

48 Y. Wang, L. Chen and W. H. K. Zhong, *J. Phys. Chem. C*, 2017, **121**, 3560.

49 X. Fan, Y. Zhang, J. Li, K. Yang, Z. Liang, Y. Chen, C. Zhao, Z. Zhang and K. Mai, *J. Mater. Chem. A*, 2018, **6**, 11664.

50 S. S. Zhang, *Energies*, 2014, **7**, 4588.

51 Y. Liu, Y. Fang, J. Qian, Z. Liu, B. Yang and X. Wang, *RSC Adv.*, 2015, **5**, 107652.

52 Y. Fu and A. Manthiram, *J. Electrochem. Soc.*, 2012, **159**, A1420.

53 N. Su, H. B. Li, S. J. Yuan, S. P. Yi and E. Q. Yin, *eXPRESS Polym. Lett.*, 2012, **6**, 697.

54 P. Arora and Z. Zhang, *Chem. Rev.*, 2004, **104**, 4419.

55 A. Yussuf, M. Al-Saleh, S. Al-Enezi and G. Abraham, *Int. J. Polym. Sci.*, 2018, **2018**, 4191747.

56 S. Chung and A. Manthiram, *J. Phys. Chem. Lett.*, 2014, **5**, 1978.

57 L. L. Kong, Z. Zhang, Y. Z. Zhang, S. Liu, G. R. Li and X. P. Gao, *ACS Appl. Mater. Interfaces*, 2016, **8**, 31684.

58 G. Li, J. Sun, W. Hou, S. Jiang, Y. Huang and J. Geng, *Nat. Commun.*, 2016, **7**, 1.

59 S. H. Chung and A. Manthiram, *Adv. Funct. Mater.*, 2014, **24**, 5299.

60 J. Qian, W. A. Henderson, W. Xu, P. Bhattacharya, M. Engelhard, O. Borodin and J. G. Zhang, *Nat. Commun.*, 2015, **6**, 6362.

61 Z. Liang, G. Zheng, C. Liu, N. Liu, W. Li, K. Yan, H. Yao, P. C. Hsu, S. Chu and Y. Cui, *Nano Lett.*, 2015, **15**, 2910.

62 G. Wang, X. Xiong, Z. Lin, J. Zheng, Z. Fenghua, Y. Li, Y. Liu, C. Yang, Y. Tang and M. Liu, *Nanoscale*, 2018, **10**, 10018.

63 J. Xie, L. Liao, Y. Gong, Y. Li, F. Shi, A. Pei, J. Sun, R. Zhang, B. Kong, R. Subbaraman, J. Christensen and Y. Cui, *Sci. Adv.*, 2017, **3**, 1.

64 R. Xu, J. Lu and K. Amine, *Adv. Energy Mater.*, 2015, **5**, 1500408.